The Astrophysical Journal, 969:42 (8pp), 2024 July 1 https://doi.org/10.3847/1538-4357/ad4d92

Low-frequency Absorption and Radio Recombination Line Features of the Galactic Center Lobe

Natasha Hurley-Walker[1], L. D. Anderson[2,3,4], M. Luisi[4,5], N. M. McClure-Griffiths[6], Robert A. Benjamin[7], Michael A. Kuhn[8], Dylan J. Linville[2,4], B. Liu[9], and Catherine Zucker[10]
[1] International Centre for Radio Astronomy Research, Curtin University, Bentley, WA 6102, Australia; nhw@icrar.org
[2] Department of Physics and Astronomy, West Virginia University, Morgantown, WV 26506, USA
[3] Adjunct Astronomer at the Green Bank Observatory, P.O. Box 2, Green Bank, WV 24944, USA
[4] Center for Gravitational Waves and Cosmology, West Virginia University, Chestnut Ridge Research Building, Morgantown, WV 26505, USA
[5] Department of Physics, Westminster College, New Wilmington, PA 16172, USA
[6] Research School of Astronomy & Astrophysics, Australian National University, Canberra 2600 ACT, Australia
[7] University of Wisconsin-Whitewater, 800 W. Main St., Whitewater, WI 53190, USA
[8] Department of Astronomy, California Institute of Technology, Pasadena, CA 91125, USA
[9] CAS Key Laboratory of FAST, National Astronomical Observatories, Chinese Academy of Sciences, Beijing 100101, People's Republic of China
[10] Harvard Astronomy, Harvard-Smithsonian Center for Astrophysics, 60 Garden St., Cambridge, MA 02138, USA
Received 2024 April 2; revised 2024 May 6; accepted 2024 May 7; published 2024 June 28

Abstract

The Galactic center lobe (GCL) is a $\sim 1^\circ$ object located north of the Galactic center. In the mid-infrared, the GCL appears as two 8.0 μm filaments that roughly define an ellipse. There is strong 24 μm and radio continuum emission in the interior of the ellipse. Due to its morphology and location in the sky, previous authors have argued that the GCL is created by outflows from star formation in the central molecular zone or by activity of the central black hole Sgr A*. We present images of the GCL from the GaLactic and Extragalactic All-sky Murchison Widefield Array survey in radio continuum that show thermal absorption against the Galactic center, incompatible with an interpretation of synchrotron self-absorption. Estimates of the cosmic-ray emissivity in this direction allow us to place a distance constraint on the GCL. To be consistent with standard emissivity assumptions, the GCL would be located 2 kpc away. At a distance of 8 kpc, the synchrotron background emissivity is enhanced by $\sim$75% in the direction of the GCL. We also present radio recombination line data from the Green Bank Telescope that constrain the electron temperature and line widths in this region, which are also more explicable if the GCL lies relatively close.

Unified Astronomy Thesaurus concepts: H II regions (694); Radio continuum emission (1340); Interstellar line emission (844); Interstellar absorption (831); Interstellar medium (847)

1. Introduction

The center of the Milky Way is home to intense star formation and a central black hole, Sgr A*, that has a mass of $4 \times 10^6\, M_\odot$ (Gillessen et al. 2009). There is little evidence that the central black hole is actively accreting. Emission from the "Fermi bubbles" (Su et al. 2010), bipolar γ-ray structures that extend some 50° above and below the plane, can be interpreted as the signature of past accretion events. An actively accreting black hole would power outflows that could be traced, for example, at radio wavelengths.

North of the Galactic center there exists a structure known as the "Galactic center lobe" (GCL), sometimes called the "Galactic center Omega lobe." The GCL is about 1° across, and roughly elliptical. If located in the Galactic center at a distance of 8.2 kpc (Abuter et al. 2019), the GCL would have a diameter of $\sim$140 pc. At mid-infrared (MIR) wavelengths, the GCL appears as two 8.0 μm filaments, with the region between them filled with 24 μm emission; thermal radio emission from plasma fills the space between the two 8.0 μm filaments.

The GCL is a conspicuous radio continuum structure that is seen in absorption at low radio frequencies. Sofue & Handa (1984) first noted the existence of the GCL in 10 GHz continuum data (see also Sofue 1985). They suggested that it was thermally emitting and hypothesized that it was created by an energetic outflow from Sgr A*. The GCL is also readily apparent in the 1.4 and 2.7 GHz continuum data of Pohl et al. (1992). The GCL may have a connection to large-scale polarized radio continuum emission (Carretti et al. 2013). Tsuboi et al. (1985) found that the eastern half of the GCL is strongly polarized, but the western half is not, which was supported by Haynes et al. (1992). Brogan et al. (2003) found free–free absorption of the GCL using multiconfiguration Very Large Array (VLA) 74 MHz data. The western part of the GCL is more strongly absorbed than the eastern half.

Multiple authors have suggested that the GCL is created by activity in the Galactic center, either due to Sgr A* (e.g., Uchida et al. 1985; Kassim et al. 1986) or due to star formation in the central molecular zone (e.g., Law et al. 2009). Law et al. (2009) detected radio recombination line (RRL) emission from the GCL using the Green Bank Telescope (GBT), which proved the existence of thermal emission. They found that the electron temperature, gas pressure, and morphology of the GCL are consistent with it being located in the Galactic center. The GCL RRL line widths are narrower than those of most Galactic H II regions, which implies low turbulence, low electron temperatures, or both. Law et al. (2009) estimated that three large star clusters in the Galactic center region could account for the ionization of the GCL.

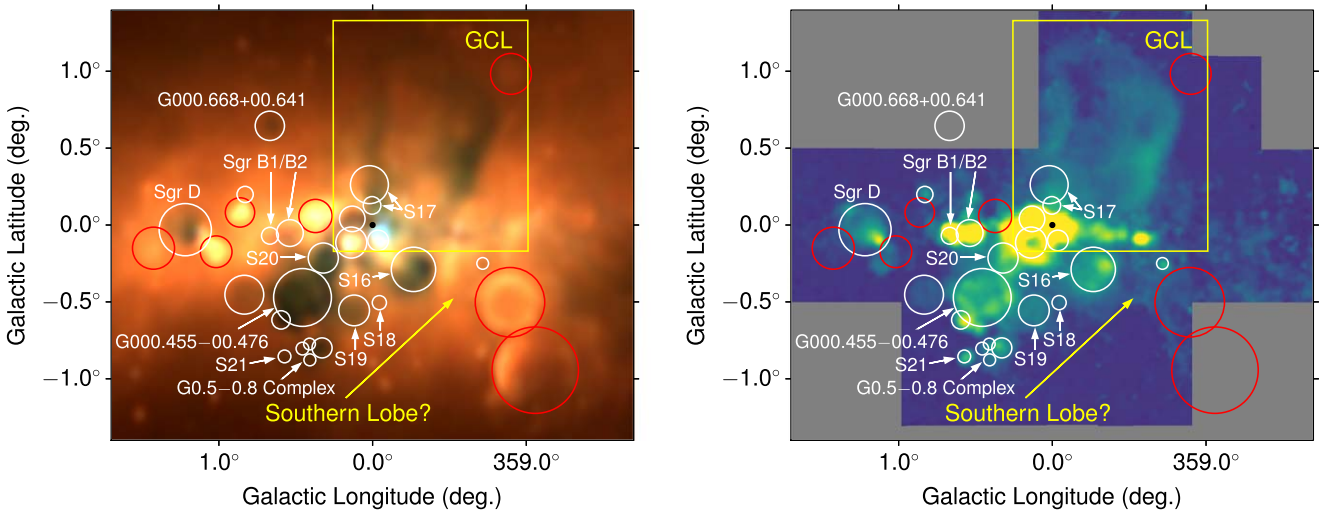

Figure 1. Overview of the Galactic center region. Left: Murchison Widefield Array GLEAM three-color image with 72–103 MHz data in red, 103–134 MHz data in green, and 139–170 MHz data in blue. Right: Green Bank Telescope GDIGS integrated Hnα RRL intensity, integrated over $\pm$20 km s^{-1}. White circles in both panels enclose particularly bright H II regions from the Wide-field Infrared Survey Explorer Catalog of Galactic H II Regions (Anderson et al. 2014) and red circles enclose known supernova remnants (Green 2006). The black dot shows the location of Sgr A*. The yellow rectangle encloses the GCL and the location of the proposed southern lobe is indicated (Bland-Hawthorn & Cohen 2003).

If the GCL is created from activity in the Galactic center, there may be a complementary feature south of the Galactic center. Bland-Hawthorn & Cohen (2003) suggested that the GCL is created by winds emanating from Sgr A* and identified a feature in Midcourse Space Experiment MIR data located south of the Galactic center. Recently, Heywood et al. (2019) observed the Galactic center with the MeerKAT radio telescope array at 1.28 MHz and 6″ angular resolution. They clearly detected the GCL, and found a complementary structure south of the Galactic center (distinct from the structure found by Bland-Hawthorn & Cohen 2003) that they posited is connected to the GCL. Heywood et al. (2019) interpret these features as arising from an explosive, energetic event near Sgr A* that occurred a few million years ago.[11] There is also X-ray emission seen toward the northern and southern features that further supports the explosion hypothesis (Nakashima et al. 2013; Ponti et al. 2019). Heywood et al. (2019) note that the southern radio continuum emission encloses the X-ray emission.

Arguments that the GCL is foreground to the Galactic center are also found in the literature. Nagoshi et al. (2019) detected RRL emission from the GCL using the Yamaguchi 32 m radio telescope and argued that the velocities of the detected thermal ionized gas are inconsistent with Galactic rotation of an object in the Galactic center (although Sofue 1996 did find evidence of fast associated molecular gas). Tsuboi et al. (2020) showed further evidence that the GCL is foreground to the Galactic center by noting that a section of the GCL is correlated with optical extinction feature while a higher-latitude section ($b > 0.8°$) is seen in Hα emission. That the GCL is seen in absorption at low radio frequencies is also evidence that it is foreground to the intense synchrotron emission found in the Galactic center (see Kassim & Weiler 1990; Brogan et al. 2003).

The data and analysis to date paint a confusing picture for the distance, size, and origin of the GCL. This paper is one of two papers that present new lines of evidence on the nature and distance of the GCL. In this paper, we examine the absorption of low radio frequencies by the structure, and its signature in radio recombination lines, to place constraints on its distance. In the companion paper we compare the MIR and radio properties of the GCL with those of Galactic H II regions.

[11] We note that the more recent data release by Heywood et al. (2022) shows the base of the GCL, but does not provide spectral index measurements of the GCL, nor imaging at higher latitudes.

2. Data

We use data from two main sources to investigate the emission of the GCL. We show overview images of the Galactic center from these data in Figure 1.

2.1. MWA GLEAM Data

The GCL was imaged by the Murchison Widefield Array (MWA; Tingay et al. 2013) between 72 and 231 MHz in 20 7.68 MHz wide subbands as part of the GaLactic and Extragalactic All-sky MWA survey (GLEAM; Wayth et al. 2015; Hurley-Walker et al. 2017, 2019). GLEAM has a resolution of $\sim$4 − 2′ over 72–231 MHz. The GLEAM data are well suited to measuring diffuse Galactic emission, as they are sensitive to angular scales of up to $\sim$30°–15° over the frequency range. At the low radio frequencies observed by the MWA, the majority of the emission from the Galactic plane is nonthermal synchrotron from cosmic rays interacting with the Galactic magnetic field. Figure 1 shows the GCL in absorption against the bright Galactic background at frequencies below $\sim$150 MHz. The strength of the absorption is correlated with the strength of RRL emission.

The GCL lies in an area of complex emission in the low-frequency radio band, so careful background subtraction is required for quantitative analyzes. We perform background subtraction individually in each GLEAM subband, and show the 76 MHz analysis in Figure 2. First, we regrid and convolve all GLEAM subband images to the same pixel grid and resolution of $5\farcm4 \times 4\farcm4$. The GLEAM maps are natively in units of Jy beam^{-1} and we convert to brightness temperature T_B in kelvins via the standard equation derived from the Rayleigh–

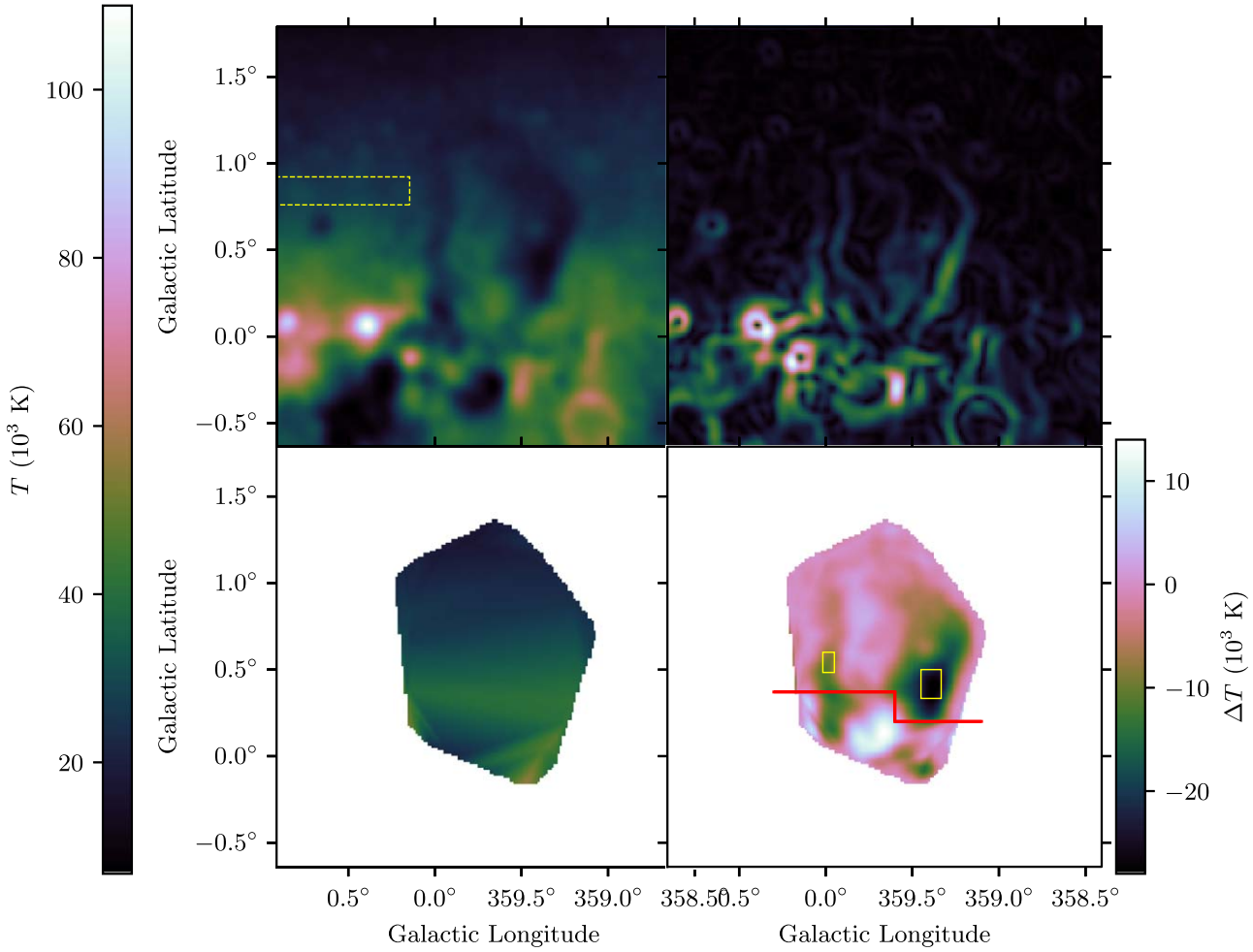

Figure 2. Background estimation and subtraction for the GLEAM 76 MHz subband. The top-left panel is the original image, centered on the GCL. The top-right panel shows the result of edge detection with a Sobel–Feldman filter. The bottom-left panel encloses the area grown by one beamwidth, and shows the background calculated by linear interpolation. The bottom-right panel shows the background-subtracted image. The dashed box in the top-left panel shows a source-free region selected to measure the rms as an input to the uncertainty calculation in Section 3. The two yellow boxes in the bottom-right panel show locations chosen to display spectral energy distributions in Section 3. The red lines in the lower right panel indicate the limit of good background subtraction sufficient to perform an absorption analysis (Section 3).

Jeans law:

$$\frac{T_B}{\mathrm{K}} = \frac{1.222 \times 10^3}{\theta_{\mathrm{maj}}\theta_{\mathrm{min}}}\left(\frac{\nu}{\mathrm{GHz}}\right)^{-2}\left(\frac{S}{\mathrm{Jy\ beam^{-1}}}\right), \quad (1)$$

where θ_{maj} and θ_{min} are the major and minor axes of the restoring beam (in radians), respectively. We use these regridded images in kelvins for all GLEAM analyzes.

We use a Sobel–Feldman operator (Sobel 1968; Duda & Hart 1973; Freeman 1990) implemented in the PYTHON package SCIPY to detect the edges of the GCL in the 76 MHz image. We then expand the edges by one beamwidth (5′), and make manual alterations to the northern border where the signal is low, creating an outline mask of the GCL. We select an area one beamwidth wide around this path to estimate the background.

For each GLEAM subband, we linearly interpolate the background path pixel values to generate a two-dimensional map of the background level across the GCL. We subtract the background maps from each subband image to produce background-subtracted images of the GCL, which are then used for analysis of the absorption (Section 3).

2.2. GBT RRL Data

We use data from the GBT Diffuse Ionized Gas Survey (GDIGS; Anderson et al. 2021), which is a fully sampled C-band (4–8 GHz) RRL survey of the inner Galactic plane using the GBT. RRLs trace the emission from thermal plasma. GDIGS simultaneously measures the emission from 22 H$n\alpha$ RRL transitions, ranging from $n = 95$ to 117, 15 of which are averaged to create final H$n\alpha$ maps of RRL emission across the Galactic plane at 2.′65 resolution.

We fit Gaussian components to data from each GDIGS spaxel that has emission of at least 3σ using GaussPy+ (Riener et al. 2019), where σ is the spectral rms computed individually from the line-free portions at each spaxel. We thereby derive the RRL line width, velocity centroid, and intensity across the GCL. This method is discussed in more detail by Anderson et al. (2021).

Using GDIGS RRL Gaussian fit parameters and the radio continuum map of Law et al. (2008), we can derive a map of T_e toward the GCL following the method of Quireza et al. (2006). The RRL and continuum data products were both created using the GBT at similar center frequencies (∼5.71 GHz for the RRL data and ∼4.85 GHz for the continuum data). Assuming that

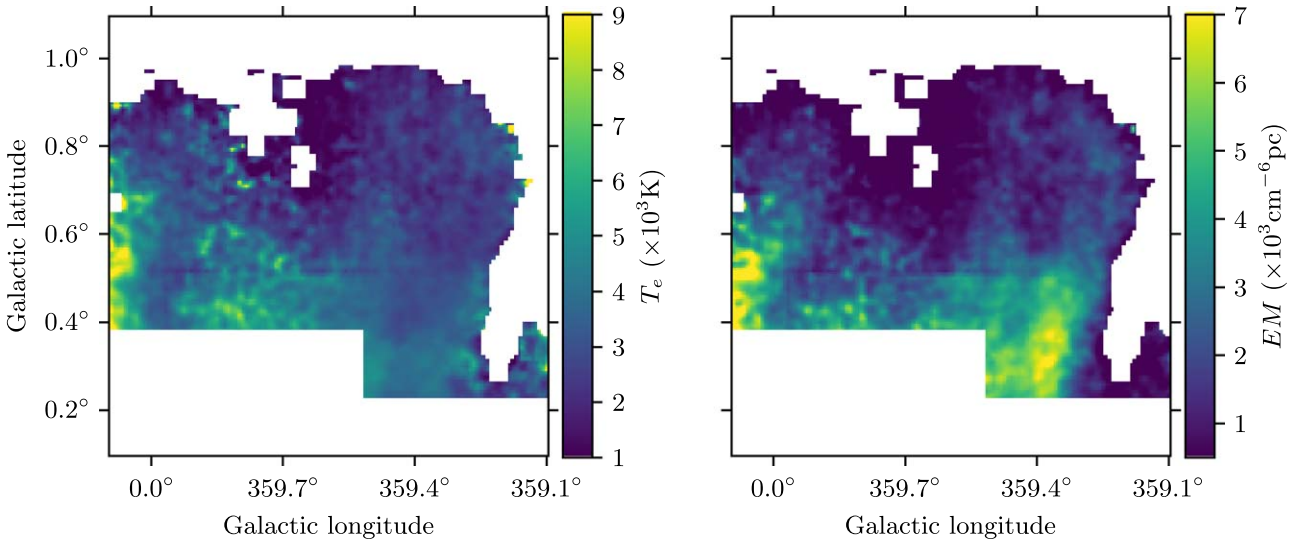

Figure 3. Electron temperature T_e (left panel) and emission measure *EM* (right panel) derived using GDIGS RRL data and radio continuum data from Law (2010). Areas not used in the analysis (see Section 3) are blanked. In areas of high signal-to-noise, $T_e \sim 3500$ K and is fairly uniform, while *EM* shows more variation, particularly with latitude.

the gas is in local thermodynamic equilibrium,

$$\left(\frac{T_{\rm e}^{*}}{\rm K}\right) = \left\{7103.3\left(\frac{\nu_{\rm L}}{\rm GHz}\right)^{1.1}\left(\frac{T_{\rm C}}{T_{\rm L}({\rm H}^{+})}\right)\left(\frac{\Delta V({\rm H}^{+})}{\rm km\,s^{-1}}\right)^{-1}(1+y^{+})^{-1}\right\}^{0.87}, \quad (2)$$

where $\nu_{\rm L} = 5.7578$ GHz is the average, $T_{\rm sys}$-weighted, frequency of our Hnα recombination lines, $T_{\rm C}$ is the continuum antenna temperature, $T_{\rm L}$ is the H line antenna temperature, $\Delta V({\rm H}^{+})$ is the hydrogen full width at half maximum (FWHM) line width, and $y^{+} = 0.03$ is the average helium-to-hydrogen ionic abundance ratio of our field of view,

$$y^{+} = \frac{T_{\rm L}({}^{4}{\rm He}^{+})\,\Delta V({}^{4}{\rm He}^{+})}{T_{\rm L}({\rm H}^{+})\,\Delta V({\rm H}^{+})}, \quad (3)$$

where $T_{\rm L}({}^{4}{\rm He}^{+})$ is the line temperature of helium and $\Delta V({}^{4}{\rm He}^{+})$ is the corresponding FWHM line width (Peimbert et al. 1992).

The strong background continuum emission near the Galactic center makes it challenging to estimate the thermal continuum associated with the GCL directly. We estimate its intensity by fitting an exponential model of the form $T_{\rm C,bg} = a_1 e^{-a_2 b} + a_0$ to the portion of the radio continuum map outside the GCL, at $\ell \approx -0.9°$ and $|b| > 0°$. In our model, $T_{\rm C,bg}$ is the background continuum temperature in kelvins and b is the Galactic latitude in degrees. We find best-fit values of $a_0 = -0.059 \pm 0.012$ K, $a_1 = 2.145 \pm 0.026$ K, and $a_2 = 4.730 \pm 0.127$ deg^{-1}. We subtract the modeled background emission from the continuum data.

We calculate $T_{\rm e}$ at each spatial location using Equation (2), with the background-subtracted continuum, the RRL intensity, and the RRL line width maps as inputs. The resulting T_e map is shown in the left panel of Figure 3. The GCL electron temperatures range from 2000 to 10,000 K, with larger $T_{\rm e}$ values found closer to the Galactic center and values of $T_e \simeq 3500$ K common for the locations of highest RRL intensity.

For optically thin Hnα GDIGS RRL emission,

$$\left(\frac{EM}{\rm cm^{-6}\,pc}\right) \simeq 0.00981\left(\frac{T_{\rm L}}{\rm K}\right)\left(\frac{\Delta V}{\rm km\,s^{-1}}\right)\left(\frac{T_{\rm e}}{\rm K}\right)^{3/2}, \quad (4)$$

where *EM* is the emission measure, T_L is the RRL amplitude, ΔV is the RRL FWHM, and T_e is the electron temperature (see the Appendix of Anderson et al. 2021). We use the intensity, line width, and T_e maps to thereby determine an emission measure map for the region, shown in the right panel of Figure 3.

2.2.1. H II Region G 000.668+00.641

Using additional GBT RRL data, we derive the electron temperature T_e and emission measure *EM* of the H II region G 000.668+00.641. This derivation is important for later analyses of the low-frequency radio emissivity (Section 3). There is Hα emission from G 000.668+00.641 (Figure 1) and therefore it is likely to be within ~2 kpc of the Sun. Because of its location off the plane, G 000.668+00.641 is relatively unconfused with other emission in the field.

We perform position-switched RRL and continuum observations of G 000.668+00.641 using the GBT at the X band (8-10 GHz), employing the same configuration and strategy as in Anderson et al. (2011) and Balser et al. (2011). We observe RRLs on-source for a total of 9 minutes at position (α, δ [J2000]) = (17:44:42.58, −28:04:24.52) and off-source for the same amount of time, following the same track in the sky. The on-source position is the location of peak intensity in the NVSS 1.4 GHz data (Condon et al. 1998). We slew across G 000.668 + 00.641 in continuum mode at a frequency of 8.665 GHz in scans of constant R.A. and decl. In total we make 10 scans across the source. The system temperature during observations was ~45 K. Calibration via noise diodes fired during observations should be good to within 10% (Balser et al. 2011), although a calibration uncertainty will affect the line and continuum data similarly.

We average all seven RRLs in the bandpass (H87α to H93α), at two polarizations, smooth to 1.9 km s^{-1} velocity

resolution, remove a polynomial baseline, and fit Gaussian components. The hydrogen RRL data are best described by a single Gaussian of height $T_L(\mathrm{H}^+) = 58.5 \pm 0.2$ mK and FWHM $\Delta V(\mathrm{H}^+) = 20.1 \pm 0.1\,\mathrm{km\,s^{-1}}$. The corresponding helium RRL fit is $T_L(^4\mathrm{He}^+) = 6.0 \pm 0.4$ mK and FWHM $\Delta V(^4\mathrm{He}^+) = 13.0 \pm 0.9\,\mathrm{km\,s^{-1}}$. The rms noise in the data is 2.816 mK, making these detections 47σ and 4.8σ, respectively (cf Lenz & Ayres 1992). The peak of hydrogen RRL emission is at $2.8 \pm 0.1\,\mathrm{km\,s^{-1}}$ (cf Lockman et al. 1996, $3.7\,\mathrm{km\,s^{-1}}$).

We average all continuum scans from a given direction and remove a polynomial baseline. The R.A. scans have a simple profile that is easily reproduced by a single Gaussian of height 352 ± 5 mK and FWHM $2.51 \pm 0.05'$. The decl. scans are more complicated, and a Gaussian fit to the peak of emission averages 372 ± 20 mK and FWHM $2.06 \pm 0.07'$. Scans from both directions peak within $0.2'$ of the targeted source position. The baseline is the largest source of uncertainty in the continuum data. Because the R.A. scan profile is much simpler than that of the decl. scan, we believe that the derived R.A.-scan parameters are closer to the true intensity, but we conservatively take the decl.-scan uncertainty. Our final continuum intensity is therefore $T_C = 350 \pm 20$ mK.

Using Equation (2), and scaling our value down by 5.7% to account for the frequency difference between line and continuum observations (Wenger et al. 2019), we find an electron temperature for G 000.668 + 00.641 of $T_e = 5700 \pm 570$ K. The emission measure is therefore $\mathrm{EM} = 8 \times 10^3\ \mathrm{cm^{-6}\,pc}$. From Equation (3), we find a value of $y^+ = 0.066 \pm 0.013$, where the 20% uncertainty is estimated from different baseline fits.

We estimate a 10% uncertainty on T_e. This estimate does not include calibration uncertainties since they will not strongly affect the ratio T_C/T_L. The continuum intensity is conservatively uncertain by about 10% due to uncertainty in determining the zero-point offset, but the RRL intensity and line widths have low uncertainties. The uncertainty of y^+ we take as 20%, but this results in only a few percent uncertainty in T_e.

3. Nature of the GCL Radio Emission

Only synchrotron self-absorption (SSA) and free–free absorption (FFA) can explain the low-frequency absorption of the GCL seen by GLEAM (Figure 1); thus, we address each in turn.

3.1. Synchrotron Self-absorption

SSA occurs when the brightness temperature of a radio source approaches the electron temperature, causing the source to become opaque. A self-absorbed synchrotron source produces brightness (and electron) temperatures of $\sqrt{1.4 \times 10^{12}(\frac{\nu}{\mathrm{Hz}})B^{-1}}$, where ν is the turnover frequency.

By extrapolating from measurements of nearby regions, Heywood et al. (2019) found that the MeerKAT 1.2 GHz radio emission of the GCL is produced by synchrotron, but they were unable to determine the spectral index from their data due to the confusing nature of the region. Law et al. (2009) analyzed GBT data at 0.33, 1.5, 5, and 8.5 GHz and also concluded that the radio continuum emission associated with the GCL is dominated by synchrotron, and that its magnetic field strength is of order 50 μG. These studies would predict that the radio continuum absorption is due to SSA.

The GLEAM data show clear absorption below $\nu = 100$ MHz, so using this frequency value and $B = 50\,\mu$G, we obtain a brightness (and electron) temperature of 1.7×10^{12} K. This value is clearly not observed; we therefore conclude that the absorption must be FFA.

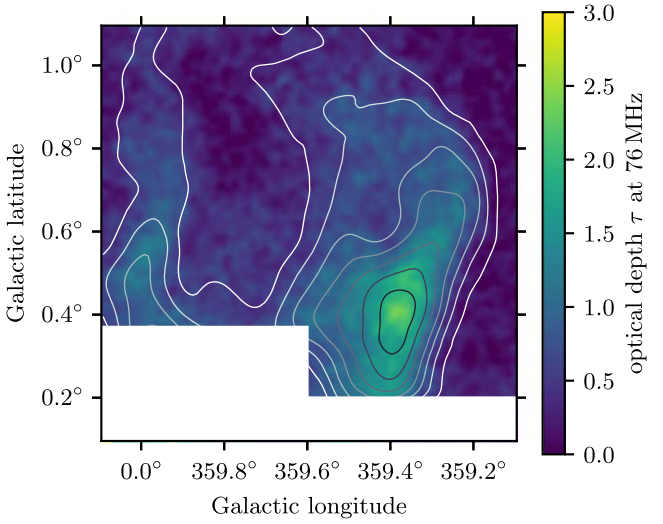

Figure 4. The optical depth at 76 MHz, calculated via Equation (6), using the *EM* and T_e shown in Figure 6. The 76 MHz GLEAM brightness temperature decrement data are overlaid using eight contours of levels -30 to -2×10^3 K, showing very similar morphology. Areas where the background subtraction of the GLEAM data were of poor quality are blanked.

3.2. Free–Free Absorption

The observed brightness temperature, T_B, toward a thermally emitting source is

$$T_B = T_e(1 - e^{-\tau(\nu)}) + T_{gb}e^{-\tau(\nu)} + T_{gf}, \quad (5)$$

where T_e is the electron temperature, T_{gb} is the temperature of the nonthermal Galactic background, T_{gf} is the temperature of the nonthermal Galactic foreground, and $\tau(\nu)$ is the optical depth. Structures dominated by the emission from thermal electrons become opaque ($\tau \geqslant 1$) at frequencies below $\sim$100 MHz, with the optical depth given by

$$\tau(\nu) \simeq 8.2 \times 10^{-2}\left(\frac{T_e}{\mathrm{K}}\right)^{-1.35}\left(\frac{\nu}{\mathrm{GHz}}\right)^{-2.1}\left(\frac{EM}{\mathrm{cm^{-6}\,pc}}\right). \quad (6)$$

The calculated optical depth at 76 MHz is shown in Figure 4. The brightness temperature decrement at 76 MHz, derived independently from the GLEAM data, is overlaid. The two maps show strong morphological similarity indicating a common origin.

From Equation (6) we expect thermal absorption to produce an exponential drop-off in radio brightness as the optical depth becomes large (at lower frequencies). We can compare the brightness temperature of the GCL as a function of frequency to that of nearby thermal and synchrotron-emitting objects. We select two regions of the GCL that have high radio continuum signal-to-noise (yellow boxes in bottom-right panel of Figure 2) and measure the average temperature as a function of frequency across the 20 background-subtracted GLEAM subband images. We compute the uncertainties at each subband from the standard deviation in the pixel values of a nearby region free of discrete sources of emission (dashed yellow box

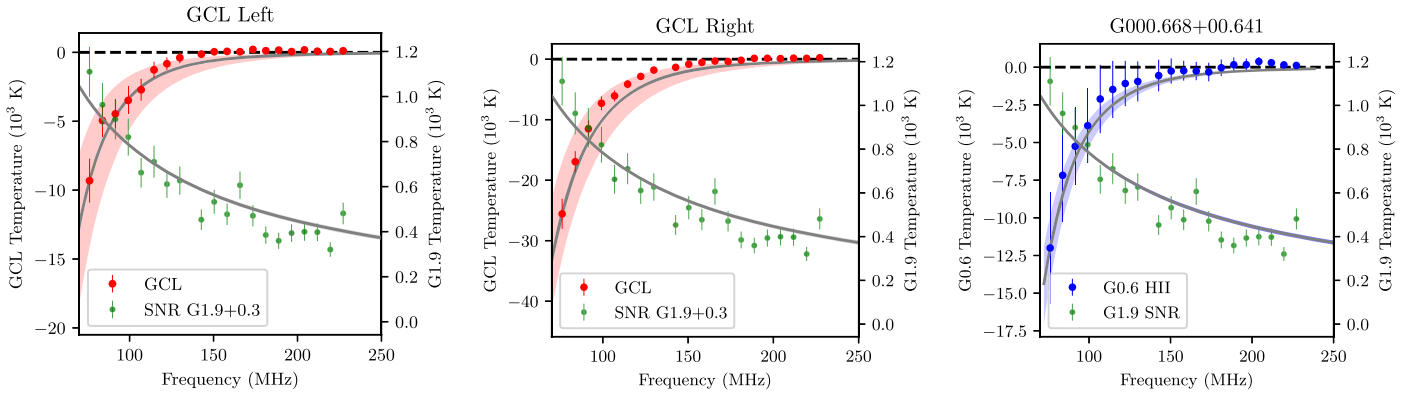

Figure 5. Temperature profiles as a function of frequency. The left panel shows the profile for the GCL region identified in the left yellow box in the bottom-right panel of Figure 2; the middle panel shows the profile for the right yellow box in the same figure; the right panel shows the profile for the H II region G 000.668 + 00.641. The red/blue points show measured temperatures from the 20 background-subtracted GLEAM subbands. The gray curves show predicted temperature profiles using the 76 MHz data and the EM and T_e values from the H II region G 000.668 + 00.641 (it is not a fit to the points). The shaded red/blue regions show the 1σ range of profile predictions given the uncertainties on the input quantities. The green points are of the SNR G 1.9 + 0.3 (Luken et al. 2020), with their derived fit as the gray curve. The SNR shows a spectrum typical of nonthermal synchrotron emission, while both lobes of the GCL and the comparison H II region show flat spectra with exponential roll-offs typical of thermal emission and free–free absorption.

in top-left panel of Figure 2), added in quadrature with a 2% calibration uncertainty (Hurley-Walker et al. 2017) and a 5% uncertainty estimated from the background subtraction process.

Using Equations (5) and (6), we derive the predicted brightness temperature as a function of frequency using the measured temperature decrement in one subband, a measurement of the emission measure, and an electron temperature. We derive the latter two quantities in Section 2.2.1 for the H II region G 000.668 + 00.641. We use the 76 MHz GLEAM subband data to derive the reference temperature decrement. This subband has the largest optical depth, so the effect of measurement errors on the derivation of the temperature profile will be minimized (since $\Delta T \propto e^{-\tau(\nu)}$).

In Figure 5 we plot the temperature (intensity) as a function of frequency for the two selected regions in the GCL (see Figure 2), with the predicted temperature curve overlaid (not fit). This shows that the low-frequency emission of the GCL is characteristic of a thermally emitting source, and not consistent with that of a nonthermal source. There is good agreement between the predicted profile and the temperature measurements. We also show the derived GLEAM brightness temperatures and the power-law fit of the nearby supernova remnant (SNR) G 1.9 + 0.3 from Luken et al. (2020). The power-law brightness distribution is typical of the synchrotron emission expected from an SNR.

We perform a similar GLEAM background subtraction to that shown in Figure 2, and derive the temperature profile of the H II region, G 000.668 + 00.641, shown in the third panel of Figure 5. These data are very similar to those of the GCL. Hindson et al. (2016) analyzed GLEAM data to show the temperature profiles of 61 H II regions, and their low-frequency radio emission profiles are similar to those of G 000.668 + 00.641 and the GCL. These comparisons show that the low-frequency emission of the GCL is consistent with that of an H II region and not consistent with that of a synchrotron-emitting object.

Based on the similarity of the GCL temperature profiles to those of G 000.668 + 00.641 and the H II regions in Hindson et al. (2016), and the dissimilarity with the temperature profile of SNR G 1.9 + 0.3, we conclude that the low-frequency emission and absorption features of the GCL are produced by thermal electrons.

4. Distance to and Emissivity toward the GCL

Thermal absorption of low-frequency radio continuum emission can be used to determine distances using the measured emissivity of the source (in in Kpc^{-1}) and the characteristic emissivity along the line of sight. Following Equation (5), if T_{gf} remains relatively constant over the field of view, one can derive the brightness temperature of the Galactic background by measuring ΔT, the difference between the temperature on-source (T_{B}) and the temperature of the background (T_{gb}):

$$\Delta T = (T_e - T_{gb})(1 - e^{-\tau(\nu)}). \quad (7)$$

One can then derive the emissivity ϵ behind the absorbing source:

$$\frac{\epsilon}{\mathrm{Kpc}^{-1}} = \frac{1}{1000}\left(\frac{T_{gb}}{\mathrm{K}}\right)\left(\frac{d_{\mathrm{edge}}}{\mathrm{kpc}}\right)^{-1}, \quad (8)$$

where d_{edge} is the distance between the H II region and the "edge" of the Galaxy. This technique was employed by Nord et al. (2006) using 74 MHz VLA observations of the inner Galaxy, and more recently by Su et al. (2017) and Su (2018) using MWA observations of a large population of Galactic H II regions. The method assumes that T_{e} and EM do not vary over the extent of the source, and that ϵ does not drastically change on angular scales smaller than the source.

We calculate the emissivity ϵ over the extent of the GCL for heliocentric distances of 2 and 8 kpc by substituting T_{gb} from Equation (7) into Equation (8), and using our measured values of T_{e}, EM, and ΔT (see Figure 6). We compare our GCL emissivity measurements to those of the nearby H II region G 000.668 + 00.641, which might be expected to have a similar background emissivity. For G 000.668 + 00.641, $T_{\mathrm{e}} = 5700 \pm 570$ K and $\mathrm{EM} = 8 \times 10^3\ \mathrm{cm}^{-6}$ pc (Section 2.2.1), and therefore τ (76 MHz) = 1.25. Based on the presence of Hα emission (Figure 1), we assume a distance to G 000.668 + 00.641 of $d = 2 \pm 1$ kpc (i.e., $d_{\mathrm{edge}} = 22 \pm 1$ kpc for a Galactic radius of 12 kpc) and measure the 76 MHz temperature difference to be $\Delta T = -12{,}000 \pm 960$ K These values yield a background 76 MHz emissivity of $\epsilon = 1.1 \pm 0.1\ \mathrm{Kpc}^{-1}$, which we show as the shaded gray horizontal bar in the top panel of Figure 6.

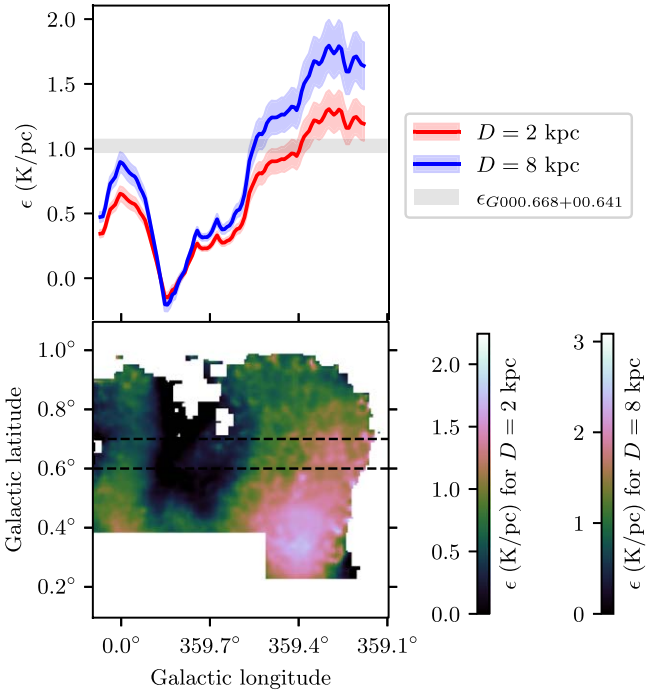

Figure 6. The derived emissivity ϵ over the GCL, using our measured values of T_e, EM, and ΔT. The bottom-left panel shows ϵ over the region where our measurements are reliable. The associated color bars show the values of ϵ for two different distance assumptions: local (2 kpc) and at the Galactic center (8 kpc). The top panel shows the average profile of the emissivity over the region $0.591^\circ < b < 0.691^\circ$, i.e., the same latitude as G 000.668 + 00.641.

The emissivity varies strongly over the GCL, with a general increase in ϵ with decreasing Galactic latitude. There is also a difference in the typical ϵ between the left and right "lobes" of the GCL (i.e., $l \approx 0^\circ$ and $l \approx 359.^\circ3$). There is no clear agreement with the background emissivity calculated from G 000.668 + 00.641, even for the same Galactic latitude range (top panel of Figure 6).

We therefore conclude that the background emissivity varies too much for this technique to place a strong constraint on the distance to the GCL. We note, however, that the values of ϵ derived for the lower distance ($d = 2$ kpc) are more consistent with the range $0.3 < \epsilon < 1.0\,\mathrm{K\,pc^{-1}}$ derived using LOFAR (Polderman et al. 2019) and the VLA (Nord et al. 2006).

5. Summary

This is one of two papers that present new evidence on the nature and distance of the GCL. Here we have shown the following:

1. The GCL has a strong turnover in the $\sim 70 - 200$ MHz GLEAM data, and this cannot be explained by synchrotron self-absorption, only free–free absorption;
2. Using RRL and radio continuum data, we measure a low and relatively consistent electron temperature across the GCL of $\lesssim 3500$ K;
3. Significant variations in emissivity are measured over the GCL on scales of $\sim 0.^\circ1$
4. Either the background emissivity is enhanced by ~ 75 % toward the GCL, or it has a distance smaller than 8 kpc, with a distance of 2 kpc being most consistent with the measurements, and other previous work.

In the companion paper we show that the GCL has infrared and radio properties similar to those of Galactic H II regions.

Acknowledgments

N.H.-W. is supported by an Australian Research Council Future Fellowship (project No. FT190100231) funded by the Australian Government. The National Radio Astronomy Observatory is a facility of the National Science Foundation operated under cooperative agreement by Associated Universities, Inc. We thank West Virginia University for its financial support of GBT operations, which enabled some of the observations for this project. This work is supported by NSF grant AST1516021 to L.D.A., NASA grant NNX17AJ27-GRAB to R.A.B., and Australian Research Council (ARC) grant DP160100723 to N.M.-G. Some of this work took part under the program SoStar of the PSI2 project funded by the IDEX Paris-Saclay, ANR-11-IDEX-0003-02. This research has made use of the SIMBAD database, operated at CDS, Strasbourg, France. R.A.B. would also like to acknowledge useful conversations on extinction distances with Gregory Green and Doug Finkbeiner.

ORCID iDs

Natasha Hurley-Walker https://orcid.org/0000-0002-5119-4808
L. D. Anderson https://orcid.org/0000-0001-8800-1793
M. Luisi https://orcid.org/0000-0001-8061-216X
N. M. McClure-Griffiths https://orcid.org/0000-0003-2730-957X
Robert A. Benjamin https://orcid.org/0000-0002-8109-2642
Michael A. Kuhn https://orcid.org/0000-0002-0631-7514
Dylan J. Linville https://orcid.org/0000-0002-4727-7619
B. Liu https://orcid.org/0000-0002-1311-8839
Catherine Zucker https://orcid.org/0000-0002-2250-730X

References

Abuter, R., Amorim, A., Bauböck, M., et al. 2019, A&A, 625, L10
Anderson, L. D., Bania, T. M., Balser, D. S., & Rood, R. T. 2011, ApJS, 194, 32
Anderson, L. D., Bania, T. M., Balser, D. S., et al. 2014, ApJS, 212, 1
Anderson, L. D., Luisi, M., Liu, B., et al. 2021, ApJS, 254, 28
Balser, D. S., Rood, R. T., Bania, T. M., & Anderson, L. D. 2011, ApJ, 738, 27
Bland-Hawthorn, J., & Cohen, M. 2003, ApJ, 582, 246
Brogan, C. L., Nord, M., Kassim, N., Lazio, J., & Anantharamaiah, K. 2003, ANS, 17, 324
Carretti, E., Crocker, R. M., Staveley-Smith, L., et al. 2013, Natur, 493, 66
Condon, J. J., Cotton, W. D., Greisen, E. W., et al. 1998, AJ, 115, 1693
Duda, R. O., & Hart, P. E. 1973, Pattern Classification and Scene Analysis (New York: Wiley), 271
Freeman, H. 1990, Machine Vision for Three-Dimensional Scenes (Amsterdam: Elsevier)
Gillessen, S., Eisenhauer, F., Trippe, S., et al. 2009, ApJ, 692, 1075
Green, D. A. 2006, A Catalog of Galactic Supernova Remnants (2006 April version) (Cambridge: Astrophysics Group, Cavendish Laboratory), http://www.mrao.cam.ac.uk/surveys/snrs/
Haynes, R. F., Stewart, R. T., Gray, A. D., et al. 1992, A&A, 264, 500
Heywood, I., Camilo, F., Cotton, W. D., et al. 2019, Natur, 573, 235
Heywood, I., Rammala, I., Camilo, F., et al. 2022, ApJ, 925, 165
Hindson, L., Johnston-Hollitt, M., Hurley-Walker, N., et al. 2016, PASA, 33, e020
Hurley-Walker, N., Callingham, J. R., Hancock, P. J., et al. 2017, MNRAS, 464, 1146
Hurley-Walker, N., Hancock, P. J., Franzen, T. M. O., et al. 2019, PASA, 36, e047
Kassim, N. E., Larosa, T. N., & Erickson, W. C. 1986, Natur, 322, 522

Kassim, N. E., & Weiler, K. W. 1990, in Lecture Notes in Physics 362, Low Frequency Astrophysics from Space; Proc. International Workshop (Berlin: Springer)
Law, C. J. 2010, ApJ, 708, 474
Law, C. J., Backer, D., Yusef-Zadeh, F., & Maddalena, R. 2009, ApJ, 695, 1070
Law, C. J., Yusef-Zadeh, F., Cotton, W. D., & Maddalena, R. J. 2008, ApJS, 177, 255
Lenz, D. D., & Ayres, T. R. 1992, PASP, 104, 1104
Lockman, F. J., Pisano, D. J., & Howard, G. J. 1996, ApJ, 472, 173
Luken, K. J., Filipović, M. D., Maxted, N. I., et al. 2020, MNRAS, 492, 2606
Nagoshi, H., Kubose, Y., Fujisawa, K., et al. 2019, PASJ, 71, 80
Nakashima, S., Nobukawa, M., & Uchida, H. 2013, ApJ, 773, 20
Nord, M. E., Henning, P. A., Rand, R. J., Lazio, T. J. W., & Kassim, N. E. 2006, AJ, 132, 242
Peimbert, M., Rodriguez, L. F., Bania, T. M., Rood, R. T., & Wilson, T. L. 1992, ApJ, 395, 484
Pohl, M., Reich, W., & Schlickeiser, R. 1992, A&A, 262, 441
Polderman, I. M., Haverkorn, M., Jaffe, T. R., & Alves, M. I. R. 2019, A&A, 621, A127
Ponti, G., Hofmann, F., Churazov, E., et al. 2019, Natur, 567, 347
Quireza, C., Rood, R. T., Bania, T. M., Balser, D. S., & Maciel, W. J. 2006, ApJ, 653, 1226
Riener, M., Kainulainen, J., Henshaw, J. D., et al. 2019, A&A, 628, A78
Sobel, I. 1968, Presentation at Stanford AI Project
Sofue, Y. 1985, PASJ, 37, 697
Sofue, Y. 1996, ApJL, 459, L69
Sofue, Y., & Handa, T. 1984, Natur, 310, 568
Su, H. 2018, MNRAS, 479, 4041
Su, H., Hurley-Walker, N., Jackson, C. A., et al. 2017, MNRAS, 465, 3163
Su, M., Slatyer, T. R., & Finkbeiner, D. P. 2010, ApJ, 724, 1044
Tingay, S. J., Goeke, R., Bowman, J. D., et al. 2013, PASA, 30, 7
Tsuboi, M., Inoue, M., Handa, T., Tabara, H., & Kato, T. 1985, PASJ, 37, 359
Tsuboi, M., Tsutsumi, T., Kitamura, Y., et al. 2020, PASJ, 72, L10
Uchida, Y., Shibata, K., & Sofue, Y. 1985, Natur, 317, 699
Wayth, R. B., Lenc, E., Bell, M. E., et al. 2015, PASA, 32, e025
Wenger, T. V., Balser, D. S., Anderson, L. D., & Bania, T. M. 2019, ApJ, 887, 114